ACS APPLIED MATERIALS & INTERFACES

www.acsami.org

Research Article

Nanoscale Heat Transport of Vertically Aligned Carbon Nanotube Bundles for Thermal Management Applications

Jean Spièce,* Kunal Lulla, Pauline de Crombrugghe de Picquendaele, Laurent Divay, Odile Bezencenet, Benoit Hackens, Pascal Gehring, Alex J. Robson, Charalambos Evangeli,* and Oleg V. Kolosov*

Cite This: *ACS Appl. Mater. Interfaces* 2024, 16, 45671−45677

Read Online

ACCESS | Metrics & More | Article Recommendations | Supporting Information

ABSTRACT: Electronic devices continue to shrink in size while increasing in performance, making excess heat dissipation challenging. Traditional thermal interface materials (TIMs) such as thermal grease and pads face limitations in thermal conductivity and stability, particularly as devices scale down. Carbon nanotubes (CNTs) have emerged as promising candidates for TIMs because of their exceptional thermal conductivity and mechanical properties. However, the thermal conductivity of CNT films decreases when integrated into devices due to defects and bundling effects. This study employs a novel cross-sectional approach combining high-vacuum scanning thermal microscopy (SThM) with beam-exit cross-sectional polishing (BEXP) to investigate the nanoscale morphology and thermal properties of vertically aligned CNT bundles at low and room temperatures. Using appropriate thermal transport models, we extracted effective thermal conductivities of the vertically aligned nanotubes and obtained 4 W m^{-1} K^{-1} at 200 K and 37 W m^{-1} K^{-1} at 300 K. Additionally, non-negligible lateral thermal conductance between CNT bundles suggests more complex heat transfer mechanisms in these structures. These findings provide unique insights into nanoscale thermal transport in CNT bundles, which is crucial for optimizing novel thermal management strategies.

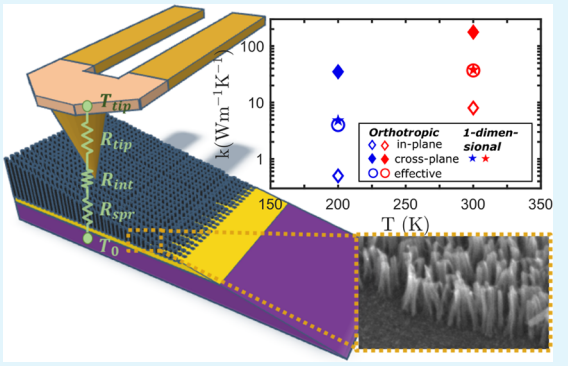

KEYWORDS: *thermal interface materials, carbon nanotubes, scanning thermal microscopy, beam-exit cross-sectional polishing, atomic force microscopy*

INTRODUCTION

While the size of electronic components is decreasing and their performance is increasing, the dissipation of excess heat is becoming a major issue for their development. This requires connecting the heat spreader of a device to the active electronic components, which can be challenging due to the device architecture, multiple hot spots, and ill-defined surfaces. Thermal interface materials (TIMs), including thermal grease, conductive adhesives, and thermal pads, are used to enhance thermal conductance between two materials.[1] However, these materials, due to their low thermal conductivity and stability, are much less efficient when scaling down devices.[2,3] For the last decades, carbon nanotubes (CNTs) have attracted great research effort for their application as TIMs thanks to their high thermal conductivity, advanced mechanical properties, and operating stability.[3−6]

The thermal conductivity of a single isolated CNT reaches very high values, in the order of a few 1000 W m^{-1} K^{-1}.[7−9] However, it dramatically decreases when several CNTs are integrated into films for potential TIM applications. Defects arising from the CNTs themselves, impurities, or coupling between the CNTs and the matrix are responsible for increasing phonon scattering and thus decreasing the effective thermal conductivity of the thermal interface material.[3−6,10] High-density vertically aligned CNTs have demonstrated a superior pathway for thermal management applications.[3] Nevertheless, in such configuration, CNTs tend to aggregate and form bundles which affect their thermal characteristics.[3−6] For example, increasing the bundle size significantly decreases the thermal conductivity compared to a single CNT.[11,12]

Using CNTs in TIMs preparation involves several manufacturing steps that drastically change the morphology and properties of its constituents. A precise knowledge of their nanoscale morphology and thermal properties is crucial to improving their functionality. Usual cross-sectional tools such as focused ion beam and transmission electron microscopy (TEM) investigations, which are suitable for such studies, require long and costly preparations that affect the properties of CNT and allow only a few μm area to be explored.

Received: May 14, 2024
Revised: July 27, 2024
Accepted: August 5, 2024
Published: August 13, 2024

To overcome these challenges, we exploited the unique ability of cross-sectional scanning thermal microscopy. This method combines a universal polishing approach, beam-exit cross-sectional polishing (BEXP)[13] with scanning thermal microscopy.[14−16] Here, BEXP creates a shallow angle beveled layer of vertically grown CNTs on the substrate with increasing length directly suitable for atomic force microscopy (AFM)-based techniques as well as scanning electron microscopy (SEM) and Raman spectroscopy studies. Compared to other cross-sectioning tools that create tiny polished regions, BEXP has the advantage of unveiling the sample internal morphology from the substrate to top over a large millimeter-sized area. This allowed us to gain morphological, mechanical, and thermal properties of the cross-sectioned CNTs. We observed bundles with a 24 nm mean diameter covering 28 ± 2% of the substrate. Moreover, we studied the thermal transport of CNTs with varying lengths at room and cryogenic temperatures by high-vacuum scanning thermal microscopy (SThM). Interestingly, we found that diffusive thermal transport mechanism is dominating in the vertically aligned CNTs bundles, even in short length bundles, with an effective thermal conductivity of 4 W m^{-1} K^{-1} at 200 K that was increased to 37 W m^{-1} K^{-1} at 300 K. Our results are confirmed by Raman spectroscopy showing that the sample is highly disordered across the whole CNTs layer.

MATERIALS AND METHODS

A forest of vertically aligned carbon nanotubes was grown on a silicon substrate. The nanotubes were synthesized using chemical vapor deposition as reported elsewhere.[17] The process requires a seed layer (SL) composed of iron catalyst on top of an aluminum oxide barrier.

After growth, the sample is polished by beam-exit cross-sectional polishing—BEXP[13,18] (Figure 1a). This nano-cross-sectioning tool creates an easily accessible wedge spanning through the whole three-dimensional (3D) structure of the sample uncovering subsurface features of the studied materials. BEXP uses three intersecting Ar-ion beams aligned to a single plane that impinge onto the side of the sample at a small negative angle (ca. −5°) from below the sample surface. The polishing terminates at close to zero (glancing) angle, which provides a polishing rate that is practically independent for diverse species.[18] Even though the BEXP method has been already applied to numerous materials,[13,18−20] we demonstrate here that it can also be applied to highly anisotropic materials and even non-fully covered surfaces.

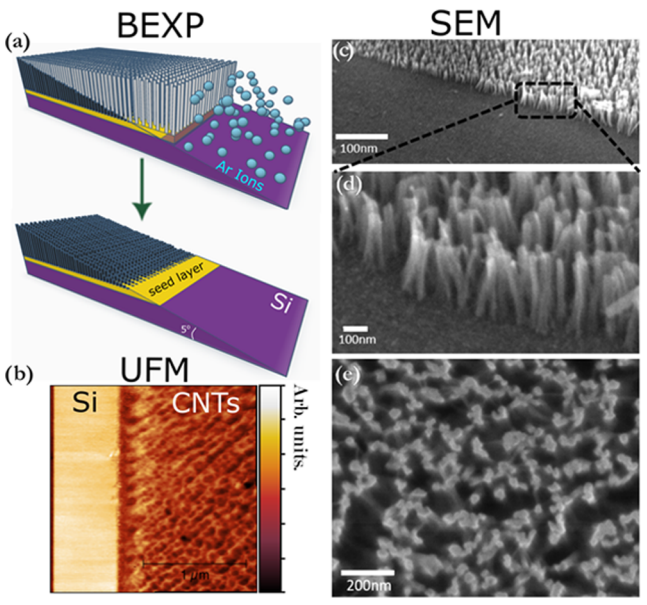

Figure 1. (a) Schematics of beam-exit cross-sectional polishing—BEXPs technique. (b) Ultrasonic force microscopy (UFM) map of the silicon-nanotubes interface. Note that stiffer areas are represented by brighter colors. (c, d) SEM images of the nanotube bundles with increasing height (c) and a zoom-in image at the same area (d). Bundles can be observed to form directly on the growth substrate. (e) Top-view SEM image showing 28 ± 2% coverage of CNTs.

For structural characterization, SEM imaging and Raman spectroscopy were employed. Nanomechanical characterization is performed with ultrasonic force microscopy (UFM), an AFM-based technique highly sensitive to surface and subsurface structures of different materials.[21−25]

Finally, to thermally characterize the CNTs forest, we use cross-sectional scanning thermal microscopy in high vacuum (~10^{-6} mbar), both at room (300 K) and cryogenic temperatures (200 K).[18,26] SThM is a scanning probe technique in which a micromachined AFM cantilever with a temperature sensor close to the tip is used to map the thermal transport in the sample. The tip highly resistive component acts as both a heating element and a temperature sensor. Thus, by monitoring the electrical resistance while raster scanning the sample, a thermal resistance map can be extracted.[26,27]

RESULTS AND DISCUSSION

In Figure 1c,d, SEM images of an array of vertically aligned CNTs with increasing height after cross-sectioning the sample are shown. Part of the sample was shaved off with an AFM tip to observe the CNTs from their side. Individual tubes can hardly be seen due to the SEM resolution. Interestingly, the vertical alignment is not affected by the BEXP process. However, as observed in Figure 1d, the CNTs form bundles consisting of several aggregated CNTs. The bundling effect begins directly at the seed layer and the average bundle diameter is 24 nm corresponding to approximately 3 nanotubes bundled together. From SEM imaging (Figure 1e), we estimate the CNT coverage area to be 28 ± 2%. We consider that the BEXP process does not create more bundling. This is visible in the SEM image in Figure 1c,d including the top area not affected by the beam due to side and negative angle of BEXP cross-sectioning that affects only the angled cut. As already mentioned, bundles are formed because of nanoparticles covering the seed layer. In continuous films, BEXP is also known to create a thin (<2 nm) amorphous layer on the polished surface.[13,18] In CNTs bundles, it is likely that the top part of the bundles also has some amorphous carbon aggregates. However, the amorphization of the bundles is considered thickness-independent, thus creating an additional interface resistance included in R_{int}.

In Figure 1b, a UFM map is shown, providing a nanomechanical understanding of the sample. A stronger signal corresponds to a stiffer material, and as it can be expected, the silicon substrate is stiffer than the nanotube bundles. Indeed, as the CNTs bending stiffness is low due to their flexibility, they deform easily under the UFM indentation. We note also that this low stiffness along the tube axis also impacts the SThM measurements of long bundles. Indeed, long bundles of over a few hundred nanometers become very floppy and hard to image with any contact mode measurement technique (see the Supporting Information, SI). This limits our analysis to tubes shorter than 250 nm.

Figure 2a,b presents the topography and thermal resistance images of the cross-sectioned area obtained simultaneously in high vacuum at 300 K. The silicon substrate and the seed layer

https://doi.org/10.1021/acsami.4c07913
ACS Appl. Mater. Interfaces 2024, 16, 45671−45677

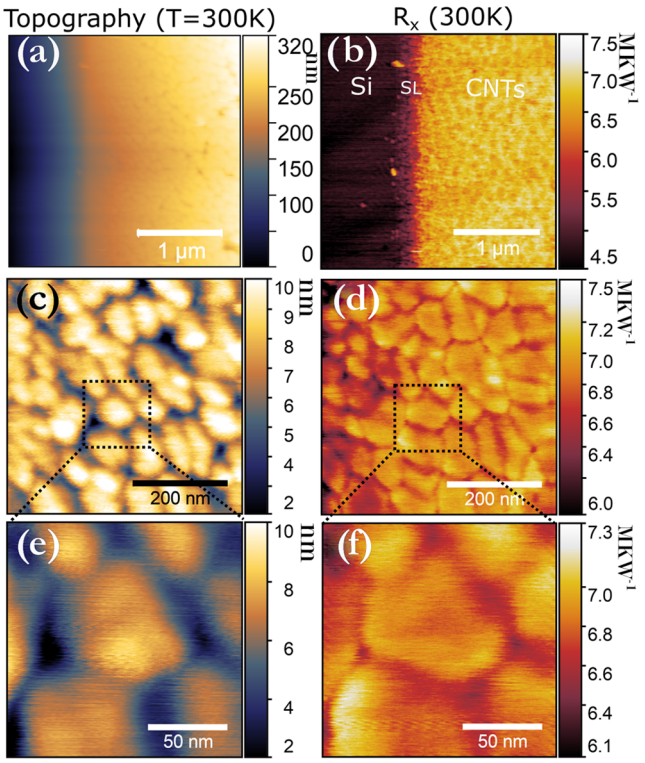

Figure 2. (a–f) Topography (a, c, e) and thermal resistance (b, d, f) maps of the cross-sectioned area at T = 300 K. Maps (e) and (f) are zoomed-in maps (c) and (d), respectively. In (a) silicon, seed layer (SL), and the CNTs are shown.

appear less thermally resistive compared to the CNTs layer. The lower thermal resistance of Si is somewhat unexpected because of the lower Si thermal conductivity compared to CNTs. There are two possible explanations for this observation. First, the thermal contact between the silicon probe and the silicon is better than the one between the probe and the bundles due to the larger mismatch between the thermal properties of CNTs and Si, and also the smaller area of contact between CNTs and the thermal probe. Second, the SThM probe is sensitive to the heat spreading resistance, not directly to the thermal conductivity. Thus, on the one hand, the bundles, as an additional layer, act as an extra resistance between the sensor and the sample heat sink and, on the other hand, the bundles provide less material for heat spreading than the silicon substrate due to the non-100% coverage.

The topography and SThM images of the CNTs forest (Figure 2c–f) confirm the bundle effect. The topography images show a distribution of bundle sizes in agreement with the SEM measurements. Furthermore, a dip is obtained between the bundles highlighting the sharpness of the probe used. The lower thermal resistance between the bundles is due to an increased contact area between the tip and the sample. As individual bundles are resolved both in topography and SThM maps, we deduce that the tip-sample contact diameter is smaller than the bundle diameter.

To compare the thermal transport of CNTs at room and low temperatures, we extract from the topography and SThM images the thermal resistance profiles along the cross-sectioned area as a function of the bundle height, t, at 200 and 300 K (see Figure 3c,d). The height is quantified from the topography since the thickness of the layer varies linearly with the position (see also the SI). The x-axis origin is located at the beginning of the vertically aligned CNTs layer for the sake of convenience. Hence, negative heights correspond to the material below the nanotubes. For both temperatures, the measured thermal resistance initially increases sharply for short nanotubes and then gradually saturates for longer CNTs. Comparing the two temperatures, we observe a giant increase in thermal resistance of CNTs, almost 1 order of magnitude at 200 K. As developed later, such an observation can be explained by a decrease of thermal conductivity at 200 K due to the suppression of phonon mode in this temperature range. An increase in the measured thermal resistance of Si substrate is also observed, which was previously attributed to the ballistic resistance increase at the tip-sample Si contact.[26] The thermal resistance obtained on the silicon substrate increases with reducing temperature, changing from 4.75 × 10^6 kW^{-1} at 300 K to 5 × 10^6 kW^{-1} at 200 K. While this is counterintuitive as

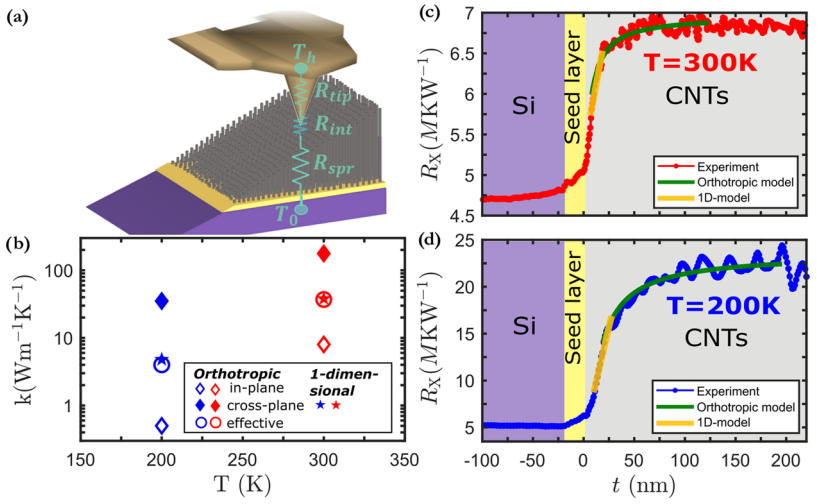

Figure 3. (a) Schematics of a thermal circuit with the resistances included between the sensor and the heat sink. T_h is the tip-heater, and T_0 is the sample temperature. (b) Thermal conductivity values as obtained with the two models for different temperatures. (c, d) Thermal resistance measured as a function of nanotubes height (t) at room (c) and low (d) temperatures and fitting of the two models applied. The R_X profiles are acquired from the SThM image by averaging 100 lines as a function of height.

https://doi.org/10.1021/acsami.4c07913
ACS Appl. Mater. Interfaces 2024, 16, 45671−45677

the silicon thermal conductivity should decrease between 200 and 300 K, it can be explained by ballistic transport aspects in the Si−Si constriction system. As reported elsewhere,[26] purely diffusive transport cannot reproduce accurately this system and ballistic aspect must be taken into account.

The saturation of the thermal resistance for longer CNTs is related to the SThM tip contact area and sample anisotropy. At 300 K, the thermal resistance saturates for CNTs longer than 75 nm, whereas at 200 K, it is almost at 150 nm, indicating an increased SThM sensitivity at lower temperatures.[26] This indicates that as the CNTs layer thickness increases, the substrate heat sink effect is less dominant in the thermal transport. At high thicknesses, the substrate becomes invisible to the thermal probe.

CNTs are attracting industrial interest for their intrinsically high thermal conductivity. However, high thermal conductivity values occur in the pristine sample and isolated tubes. These high values mean that the phonon mean path can reach a length as long as 1 μm.[28] Ballistic transport has been observed in stand-alone individual CNTs with lengths comparable to the phonon mean free path.[29] In our case, both bundling effect and interbundle contact as well as the temperature regime of the experiment are expected to increase phonon scattering processes, therefore greatly reducing the phonon mean free path (l).[30−32] However, at lower temperatures, the l in CNTs is expected to increase.[32] A simple way to account for mixed ballistic-diffusive transport is to add both components as in $R = R_{\text{ballistic}} + R_{\text{diffusive}}$[33] or equivalent write[34,35]

$$R = R_{\text{ballistic}}\left(1 + \frac{L}{l}\right) \tag{1}$$

Thermal transport is ballistic when $l \gg L$ and thermal conductivity increases linearly with the length, while thermal resistance remains constant. When $l < L$ diffusive transport contribution becomes more important and finally for very large L, such as $l \ll L$, it dominates. For diffusive transport, the thermal conductivity becomes length-independent, while thermal resistance increases with length. Considering that $R_{\text{tip}} + R_{\text{int}}$ is constant for different lengths, the evolution of R_X with L can give information for the transport nature in our system. The overall increase of R_X with length for CNTs longer than 15 nm indicates a dominant diffusive transport contribution. The diffusive nature of the transport for CNTs is also supported by an additional modeling procedure that we applied to our data (see the SI).

To quantitatively extract the thermal properties of CNTs, we consider a diffusive thermal transport mechanism. We express R_X as a sum of thermal resistances of the conical tip itself R_{tip}, the tip apex-sample interface (R_{int}), and the spreading resistance inside the sample R_{spr} (see also Figure 3a):

$$R_X(t) = R_{\text{tip}} + R_{\text{int}} + R_{\text{spr}}(t) \tag{2}$$

where R_{tip} is expected to be constant for all of the different parts of the sample, while R_{int} is likely to change drastically between the tip−Si substrate and the tip−nanotubes contacts as previously discussed. However, we can assume that while scanning within the same material, for example, the nanotubes only, R_{int} remains constant and therefore the sum $R_{\text{tip}} + R_{\text{int}}$ can be considered constant.

We apply two different diffusive transport models describing R_{spr} of the cross-sectioned CNTs, namely, one-dimensional (1D) and orthotropic, respectively. The first model considers the sample as an array of vertically aligned cylinders and assumes one-dimensional (1D) transport along these cylinders. The thermal resistance can be written as a function of the bundle height L_{bundle}:

$$R_{\text{bundle}} = \frac{L_{\text{bundle}}}{k_{\text{bundle}}A} \tag{3}$$

where A and k_{bundle} are the cross-sectional area and thermal conductivity of the bundle, respectively. Cross-sectional area is ill-defined in the case of a single nanotube and thus for nanotube bundles. For a single tube, it can be defined as $A = \pi d\delta$, with d being the tube diameter and δ being the layer separation of graphite. However, as in our case we are dealing with bundles, we consider the bundles as isotropic materials and as such we find a lower bound of the thermal conductivity.

R_X saturates for longer CNTs (at around 75 and 150 nm for 200 and 300 K, respectively), highlighting the fact that heat spreading also occurs perpendicularly to the CNT axis. Therefore, to model our samples as an array of cylinders, we use only the transition part between 10 and 30 nm (see the yellow line in Figure 3c,d). It has been shown that the thermal conductivity of a single nanotube can be considered constant when it reaches 15 nm length.[30] Considering this region, we obtained a roughly linear trend with the height of the tubes; the derivative of the thermal resistance measured should compare to dR_{bundle}/dL. More importantly, this derivative does not depend on the tip-sample interface resistance ($R_{\text{tip}} + R_{\text{int}}$), contact area, and interface contact resistance at the tube−substrate interface.

The second model considers anisotropic heat transport in the CNTs area, with high thermal conductivity along the bundle axis, $k_{\parallel}$, and a low thermal conductivity perpendicularly, $k_{\perp}$. This allows us to use a model for R_{spr} of layered material on a substrate and for a heat source of radius a.[16,18,36−38] In particular, it transforms the directional-dependent thermal conductivities ($k_{\perp}$, $k_{\parallel}$) of the layer to an effective isotropic thermal conductivity (k_{eff}) which includes the layer−substrate interface resistance (r_{int}) with thickness (t_{eff}) larger than the real thickness of the layer.[39] The layer−substrate interface resistance r_{int} includes contributions from the seed layer and the CNTs interfaces. Finally, R_{spr} is given by

$$R_{\text{spr}}(t) = \frac{1}{\pi k_{\text{eff}} a}\int_0^{\infty}\left[\frac{1 + K\exp\left(\frac{-2\xi t_{\text{eff}}}{a}\right)}{1 - K\exp\left(\frac{-2\xi t_{\text{eff}}}{a}\right)}\right]J_1(\xi)\sin(\xi)\frac{d\xi}{\xi^2} \tag{4}$$

where ξ is the Bessel function, $k_{\text{eff}} = \sqrt{(k_{\perp}k_{\parallel})}$, $t_{\text{eff}} = \sqrt{(k_{\parallel}/k_{\perp})}t + r_{\text{int}}k_{\text{eff}}$, and $K = \frac{1 - k_{\text{sub}}/k_{\text{eff}}}{1 + k_{\text{sub}}/k_{\text{eff}}}$, with k_{sub} being the substrate thermal conductivity.

We estimate a tip-sample contact diameter of 8 ± 4 nm from the resistance measured on the silicon substrate (see the SI for details). We fit the experimental data with $R_{\text{tip}} + R_{\text{int}}$, r_{int}, $k_{\perp}$, and $k_{\parallel}$ being the fitting parameters (see green line in Figure 3c,d). Note that this model considers a uniform layer on a substrate which is not the case of the CNT layer, as bundles are not fully covering the surface. Therefore, r_{int} and $k_{\parallel}$ need to be normalized to the CNTs coverage (28 ± 2%). However, this normalization is not necessary for the one-dimensional

https://doi.org/10.1021/acsami.4c07913
ACS Appl. Mater. Interfaces 2024, 16, 45671−45677

heat transport, in which we considered that the tip contacts a single bundle and measures a resistance variation from the bundle length change.

The thermal conductivity values obtained with the two models are summarized in Figure 3b and explicitly written in the SI. We find good agreement of k_{bundle} and k_{eff} as obtained by the 1D- and the orthotropic model, respectively. The slightly higher values along the bundle axis for the orthotropic model at both temperatures is coherent as perpendicular transport is also considered in this model. Comparing the values for the 2 different temperatures, we see that the ones obtained at 200 K are lower than the ones obtained at room temperature. The increased thermal conductivity with temperature at this range is in line with previous works. At low temperatures, thermal conductivity increases with temperature due to the activation of additional phonon modes up to reach a maximum value around room temperature. For higher temperatures, it decreases due to increased scattering.[8,40,41] Another observation is that the thermal conductivity anisotropy decreases with temperature. The anisotropy ratio ($k_{\parallel}/k_{\perp}$) goes from 22 at 300 K to 8 at 200 K. Similar reduction has been observed by Yamaguchi et al.[42] We attribute it to both a strong reduction of the innertube thermal conductivity and a stiffening of the nanotubes at low temperature.[43]

Finally, we compare the thermal conductivity values obtained in this work with those in the literature for similar CNTs bundles. Overall, our values are smaller than those reported for bundles of similar diameter. Feng et al. reported thermal conductivities of 100 and 110 W m^{-1} K^{-1} at T = 200 and 300 K, respectively, for a bundle of 13 nanotubes and 450 and 1600 W m^{-1} K^{-1} for a 3 CNT bundles at the same temperatures.[11] Shi et al. on the other hand for 10 nm diameter bundle reported 130 and 215 W m^{-1} K^{-1} for T = 200 and 300 K, respectively.[12] Furthermore, for bundle of diameter 10.3 nm and 14.3 μm length, the thermal conductivity is found to be 253 W m^{-1} K^{-1}.[44] Theoretical simulations predicted values ranging from 950 and 5.6[45] to 0.55 and 0.028 W m^{-1} K^{-1},[46] along and across the bundle, respectively. The lower values we observe, in comparison to the literature, can be attributed to increased phonon scattering inside the CNT bundles and between the bundles. This is confirmed by the Raman spectrum measured in the cross-sectioned area, showing a high level of disorder in the sample compared to high-quality crystalline nanotubes (see Supporting Information, Section S5). Regarding the anisotropy we measured, we obtained a ratio of 22 at 300 K and 8 at 200 K. Such high ratios have been reported for nanotubes and two-dimensional (2D) materials. For example, graphite has high anisotropy over 100.[47] Similarly, for MoS_2, the in-plane thermal conductivity was found 50 times larger than the cross-plane by Liu et al.[48] For ReS_2, the anisotropy reaches 130,[49] and for $SnSe_2$, the anisotropy ratio was found around 8.4.[50] For carbon nanotubes, anisotropy ratio can reach extremely high values up of several hundred.[42,51] The anisotropy can even be tuned depending on the nanotube alignment configuration.[52]

CONCLUSIONS

In conclusion, we performed thermal transport measurements on a unique sample composed of length increasing CNT bundles at high vacuum at 200 and 300 K. The sample was prepared by BEXP and allowed shallow angle polishing. As the nanotubes kept their structure and alignment after the polishing, this opens new perspectives of materials study. A drastic increase in the thermal resistance with reducing temperature was measured, which is related to the reducing CNT thermal conductivity. Two coherent diffusive modeling procedures were applied and obtained an effective thermal conductivity of 4 and 37 W m^{-1} K^{-1} at 200 and 300 K, respectively. The thermal anisotropy was estimated using an orthotropic model accounting for the thermal conductivity along and perpendicular to the bundle axis taking into account the measured CNT coverage of the sample. Significantly, we found non-negligible lateral thermal conductance between the nanotube bundles. This study presents a new perspective for investigating vertical structures. It also provides information about the temperature dependence of the nanoscale thermal transport of vertically aligned CNT bundles.

ASSOCIATED CONTENT

Supporting Information

The Supporting Information is available free of charge at https://pubs.acs.org/doi/10.1021/acsami.4c07913.

Topography and thermal resistance maps, UFM maps, modeling details including tip-sample contact diameter estimation, thermal conductivities from diffusive transport models and ballistic heat transport modeling, and Raman spectra (PDF)

AUTHOR INFORMATION

Corresponding Authors

Jean Spièce − *IMCN/NAPS, UCLouvain, B-1348 Louvain-la-Neuve, Belgium; Physics Department, Lancaster University, LA1 4YB Lancaster, U.K.;* orcid.org/0000-0002-2433-6348; Email: jean.spiece@uclouvain.be

Charalambos Evangeli − *Physics Department, Lancaster University, LA1 4YB Lancaster, U.K.; Department of Materials, University of Oxford, OX1 3PH Oxford, U.K.;* orcid.org/0000-0003-3867-8530; Email: ch.evangeli@gmail.com

Oleg V. Kolosov − *Physics Department, Lancaster University, LA1 4YB Lancaster, U.K.;* orcid.org/0000-0003-3278-9643; Email: o.kolosov@lancaster.ac.uk

Authors

Kunal Lulla − *Physics Department, Lancaster University, LA1 4YB Lancaster, U.K.; National Graphene Institute, The University of Manchester, M13 9PL Manchester, U.K.*

Pauline de Crombrugghe de Picquendaele − *IMCN/NAPS, UCLouvain, B-1348 Louvain-la-Neuve, Belgium*

Laurent Divay − *Thales Research and Technology, 91767 Palaiseau, France*

Odile Bezencenet − *Thales Research and Technology, 91767 Palaiseau, France*

Benoit Hackens − *IMCN/NAPS, UCLouvain, B-1348 Louvain-la-Neuve, Belgium;* orcid.org/0000-0001-6121-5126

Pascal Gehring − *IMCN/NAPS, UCLouvain, B-1348 Louvain-la-Neuve, Belgium;* orcid.org/0000-0002-7073-9922

Alex J. Robson − *Physics Department, Lancaster University, LA1 4YB Lancaster, U.K.*

Complete contact information is available at: https://pubs.acs.org/10.1021/acsami.4c07913

Notes

The authors declare no competing financial interest.

■ ACKNOWLEDGMENTS

O.V.K., C.E., and J.S. acknowledge the support of the EU grant QUANTIHEAT (project 604668). The authors acknowledge helpful scientific support and discussion of Jean-Christophe Charlier and Severine Gomez. P.G. and J.S. acknowledge financial support from the F.R.S.-FNRS of Belgium (FNRS-CQ-1.C044.21-SMARD, FNRS-CDR-J.0068.21-SMARD, FNRS-MIS-F.4523.22-TopoBrain, FNRS-PDR-T.0128.24-ART-MULTI, FNRS-CR-1.B.463.22-MouleFrits, FNRS-PDR-T.0029.22-Moiré). P.G. acknowledges financial support from the EU (ERC-StG-10104144-MOUNTAIN), from the Federation Wallonie-Bruxelles through the ARC Grant No. 21/26-116, and from the FWO and FRS-FNRS under the Excellence of Science (EOS) program (40007563-CONNECT). O.V.K. acknowledges the support of the European Graphene Flagship Core3 project (grant agreement no. 881603), EPSRC EP/V00767X/1 HiWiN project, and UKRI Nexgenna project.

■ REFERENCES

(1) Razeeb, K. M.; Dalton, E.; Cross, G. L. W.; Robinson, A. J. Present and future thermal interface materials for electronic devices. *Int. Mater. Rev.* **2018**, *63*, 1−21.

(2) Prasher, R. Thermal interface materials: historical perspective, status, and future directions. *Proc. IEEE* **2006**, *94*, 1571−1586.

(3) Yuan, G.; Li, H.; Shan, B.; Liu, J. Thermal Interface materials based on vertically aligned carbon nanotube arrays: a review. *Micro Nanosyst.* **2019**, *11*, 3−10.

(4) Xu, J.; Fisher, T. S. Enhancement of thermal interface materials with carbon nanotube arrays. *Int. J. Heat Mass Transfer* **2006**, *49*, 1658−1666.

(5) McNamara, A. J.; Joshi, Y.; Zhang, Z. M. Thermal resistance of thermal conductive adhesive anchored carbon nanotubes interface material. *Int. J. Therm. Sci.* **2015**, *96*, 221−226.

(6) Ni, Y.; Le Khanh, H.; Chalopin, Y.; Bai, J.; Lebarny, P.; Divay, L.; Volz, S. Highly efficient thermal glue for carbon nanotubes based on azide polymers. *Appl. Phys. Lett.* **2012**, *100*, No. 193118.

(7) Pettes, M. T.; Shi, L. Thermal and structural characterizations of individual single-, double-, and multi-walled carbon nanotubes. *Adv. Funct. Mater.* **2009**, *19*, 3918−3925.

(8) Pop, E.; Mann, D.; Wang, Q.; Goodson, K.; Dai, H. Thermal conductance of an individual single-wall carbon nanotube above room temperature. *Nano Lett.* **2006**, *6*, 96−100.

(9) Hone, J.; Whitney, M.; Piskoti, C.; Zettl, A. Thermal conductivity of single-walled carbon nanotubes. *Phys. Rev. B* **1999**, *59*, R2514.

(10) Jones, R. S.; Gonzalez-Munoz, S.; Griffiths, I.; Holdway, P.; Evers, K.; Luanwuthi, S.; Maciejewska, B. M.; Kolosov, O.; Grobert, N. Thermal conductivity of carbon/boron nitride heteronanotube and boron nitride nanotube Buckypapers: Implications for thermal management composites. *ACS Appl. Nano Mater.* **2023**, *6*, 15374−15384.

(11) Feng, Y.; Inoue, T.; An, H.; Xiang, R.; Chiashi, S.; Maruyama, S. Quantitative study of bundle size effect on thermal conductivity of single-walled carbon nanotubes. *Appl. Phys. Lett.* **2018**, *112*, No. 191904.

(12) Shi, L.; Li, D.; Yu, C.; Jang, W.; Kim, D.; Yao, Z.; Kim, P.; Majumdar, A. Measuring thermal and thermoelectric properties of one-dimensional nanostructures using a microfabricated device. *J. Heat Transfer* **2003**, *125*, 881−888.

(13) Robson, A. J.; Grishin, I.; Young, R. J.; Sanchez, A. M.; Kolosov, O. V.; Hayne, M. High-accuracy analysis of nanoscale semiconductor layers using beam-exit ar-ion polishing and scanning probe microscopy. *ACS Appl. Mater. Interfaces* **2013**, *5*, 3241−3245.

(14) Tovee, P.; Pumarol, M.; Zeze, D.; Kjoller, K.; Kolosov, O. Nanoscale spatial resolution probes for scanning thermal microscopy of solid state materials. *J. Appl. Phys.* **2012**, *112*, No. 114317.

(15) Gomès, S.; Assy, A.; Chapuis, P.-O. Scanning thermal microscopy: A review. *Phys. Status Solidi A* **2015**, *212*, 477−494.

(16) Gonzalez-Munoz, S.; Agarwal, K.; Castanon, E. G.; Kudrynskyi, Z. R.; Kovalyuk, Z. D.; Spièce, J.; Kazakova, O.; Patanè, A.; Kolosov, O. V. Direct Measurements of Anisotropic Thermal Transport in γ-InSe Nanolayers via Cross-Sectional Scanning Thermal Microscopy. *Adv. Mater. Interfaces* **2023**, *10*, No. 2300081.

(17) Nylander, A.; Hansson, J.; Kabiri Samani, M.; Chandra Darmawan, C.; Borta Boyon, A.; Divay, L.; Ye, L.; Fu, Y.; Ziaei, A.; Liu, J. Reliability investigation of a carbon nanotube array thermal Interface material. *Energies* **2019**, *12*, 2080.

(18) Spièce, J.; Evangeli, C.; Robson, A. J.; El Sachat, A.; Haenel, L.; Alonso, M. I.; Garriga, M.; Robinson, B. J.; Oehme, M.; Schulze, J.; Alzina, F.; Sotomayor Torres, C.; Kolosov, O. V. Quantifying thermal transport in buried semiconductor nanostructures via cross-sectional scanning thermal microscopy. *Nanoscale* **2021**, *13*, 10829−10836.

(19) Pandey, K.; Paredis, K.; Robson, A. J.; Vandervorst, W. Understanding the effect of confinement in scanning spreading resistance microscopy measurements. *J. Appl. Phys.* **2020**, *128*, No. 034303.

(20) Pan, H.; Chen, Y.; Pang, W.; Sun, H.; Li, J.; Lin, Y.; Kolosov, O.; Huang, Z. Complementary sample preparation strategies (PVD/BEXP) combining with multifunctional SPM for the characterizations of battery interfacial properties. *MethodsX* **2021**, *8*, No. 101250.

(21) Oleg Kolosov, O. K.; Yamanaka, K. Nonlinear detection of ultrasonic vibrations in an atomic force microscope. *Jpn. J. Appl. Phys.* **1993**, *32*, L1095.

(22) Robinson, B. J.; Giusca, C. E.; Gonzalez, Y. T.; Kay, N. D.; Kazakova, O.; Kolosov, O. V. Structural, optical and electrostatic properties of single and few-layers MoS2: effect of substrate. *2D Mater.* **2015**, *2*, No. 015005.

(23) Bosse, J. L.; Tovee, P.; Huey, B.; Kolosov, O. Physical mechanisms of megahertz vibrations and nonlinear detection in ultrasonic force and related microscopies. *J. Appl. Phys.* **2014**, *115*, No. 144304.

(24) El Sachat, A.; Spiece, J.; Evangeli, C.; Robson, A. J.; Kreuzer, M.; Rodriguez-Laguna, M. R.; Chavez, E.; Sledzinska, M.; Sotomayor Torres, C. M.; Kolosov, O. V.; Alzina, F. Nanoscale mapping of thermal and mechanical properties of bare and metal-covered self-assembled block copolymer thin films. *ACS Appl. Polym. Mater.* **2020**, *2*, 487−496.

(25) Spiece, J.; Sangtarash, S.; Mucientes, M.; Molina-Mendoza, A. J.; Lulla, K.; Mueller, T.; Kolosov, O.; Sadeghi, H.; Evangeli, C. Low thermal conductivity in franckeite heterostructures. *Nanoscale* **2022**, *14*, 2593−2598.

(26) Evangeli, C.; Spiece, J.; Sangtarash, S.; Molina-Mendoza, A. J.; Mucientes, M.; Mueller, T.; Lambert, C.; Sadeghi, H.; Kolosov, O. Nanoscale Thermal Transport in 2D Nanostructures from Cryogenic to Room Temperature. *Adv. Electron. Mater.* **2019**, *5*, No. 1900331.

(27) Spiece, J.; Evangeli, C.; Lulla, K.; Robson, A.; Robinson, B.; Kolosov, O. Improving accuracy of nanothermal measurements via spatially distributed scanning thermal microscope probes. *J. Appl. Phys.* **2018**, *124*, No. 015101.

(28) Bulmer, J. S.; Kaniyoor, A.; Elliott, J. A. A meta-analysis of conductive and strong carbon nanotube materials. *Adv. Mater.* **2021**, *33*, No. 2008432.

(29) Chiu, H.-Y.; Deshpande, V.; Postma, H. C.; Lau, C.; Miko, C.; Forro, L.; Bockrath, M. Ballistic phonon thermal transport in multiwalled carbon nanotubes. *Phys. Rev. Lett.* **2005**, *95*, No. 226101.

(30) Yang, D. J.; Zhang, Q.; Chen, G.; Yoon, S. F.; Ahn, J.; Wang, S. G.; Zhou, Q.; Wang, Q.; Li, J. Q. Thermal conductivity of multiwalled carbon nanotubes. *Phys. Rev. B* **2002**, *66*, No. 165440.

(31) Kim, P.; Shi, L.; Majumdar, A.; McEuen, P. L. Thermal transport measurements of individual multiwalled nanotubes. *Phys. Rev. Lett.* **2001**, *87*, No. 215502.

https://doi.org/10.1021/acsami.4c07913
ACS Appl. Mater. Interfaces 2024, 16, 45671−45677

(32) Marconnet, A. M.; Panzer, M. A.; Goodson, K. E. Thermal conduction phenomena in carbon nanotubes and related nanostructured materials. *Rev. Mod. Phys.* **2013**, *85*, 1295.
(33) Siemens, M. E.; Li, Q.; Yang, R.; Nelson, K. A.; Anderson, E. H.; Murnane, M. M.; Kapteyn, H. C. Quasi-ballistic thermal transport from nanoscale interfaces observed using ultrafast coherent soft X-ray beams. *Nat. Mater.* **2010**, *9*, 26−30.
(34) Yamamoto, T.; Konabe, S.; Shiomi, J.; Maruyama, S. Crossover from ballistic to diffusive thermal transport in carbon nanotubes. *Appl. Phys. Express* **2009**, *2*, No. 095003.
(35) Mingo, N.; Broido, D. Length dependence of carbon nanotube thermal conductivity and the "problem of long waves". *Nano Lett.* **2005**, *5*, 1221−1225.
(36) Muzychka, Y. S.; Yovanovich, M.; Culham, J. Thermal spreading resistance in compound and orthotropic systems. *J. Thermophys. Heat Transfer* **2004**, *18*, 45−51.
(37) Ahmad, M.; Agarwal, K.; Munoz, S. G.; Ghosh, A.; Kodan, N.; Kolosov, O. V.; Mehta, B. R. Engineering interfacial effects in electron and phonon transport of Sb2Te3/MoS2 multilayer for thermoelectric ZT above 2.0. *Adv. Funct. Mater.* **2022**, *32*, No. 2206384.
(38) Maiti, A.; Agarwal, K.; Gonzalez-Munoz, S.; Kolosov, O. V. Quantifying anisotropic thermal transport in two-dimensional perovskite (PEA 2 PbI 4) through cross-sectional scanning thermal microscopy. *Phys. Rev. Mater.* **2023**, *7*, No. 023801.
(39) Menges, F.; Riel, H.; Stemmer, A.; Dimitrakopoulos, C.; Gotsmann, B. Thermal transport into graphene through nanoscopic contacts. *Phys. Rev. Lett.* **2013**, *111*, No. 205901.
(40) Kwon, Y.-K.; Kim, P. *High Thermal Conductivity Materials*; Springer, 2006; pp 227−265.
(41) Yu, C.; Shi, L.; Yao, Z.; Li, D.; Majumdar, A. Thermal conductance and thermopower of an individual single-wall carbon nanotube. *Nano Lett.* **2005**, *5*, 1842−1846.
(42) Yamaguchi, S.; Tsunekawa, I.; Komatsu, N.; Gao, W.; Shiga, T.; Kodama, T.; Kono, J.; Shiomi, J. One-directional thermal transport in densely aligned single-wall carbon nanotube films. *Appl. Phys. Lett.* **2019**, *115*, No. 223104.
(43) Zhang, C.; Song, Y.; Zhang, H.; Lv, B.; Qiao, J.; Yu, N.; Zhang, Y.; Di, J.; Li, Q. Mechanical properties of carbon nanotube fibers at extreme temperatures. *Nanoscale* **2019**, *11*, 4585−4590.
(44) Hsu, I.-K.; Pettes, M. T.; Bushmaker, A.; Aykol, M.; Shi, L.; Cronin, S. B. Optical absorption and thermal transport of individual suspended carbon nanotube bundles. *Nano Lett.* **2009**, *9*, 590−594.
(45) Che, J.; Cagin, T.; Goddard III, W. A. Thermal conductivity of carbon nanotubes. *Nanotechnology* **2000**, *11*, 65.
(46) Evans, W. J.; Shen, M.; Keblinski, P. Inter-tube thermal conductance in carbon nanotubes arrays and bundles: Effects of contact area and pressure. *Appl. Phys. Lett.* **2012**, *100*, No. 261908.
(47) Pop, E.; Varshney, V.; Roy, A. K. Thermal properties of graphene: Fundamentals and applications. *MRS Bull.* **2012**, *37*, 1273−1281.
(48) Liu, J.; Choi, G.-M.; Cahill, D. G. Measurement of the anisotropic thermal conductivity of molybdenum disulfide by the time-resolved magneto-optic Kerr effect. *J. Appl. Phys.* **2014**, *116*, No. 233107.
(49) Jang, H.; Ryder, C. R.; Wood, J. D.; Hersam, M. C.; Cahill, D. G. 3D anisotropic thermal conductivity of exfoliated rhenium disulfide. *Adv. Mater.* **2017**, *29*, No. 1700650.
(50) Xiao, P.; Chavez-Angel, E.; Chaitoglou, S.; Sledzinska, M.; Dimoulas, A.; Sotomayor Torres, C. M.; El Sachat, A. Anisotropic thermal conductivity of crystalline layered SnSe2. *Nano Lett.* **2021**, *21*, 9172−9179.
(51) Hamasaki, H.; Takimoto, S.; Hirahara, K. Visualization of thermal transport within and between carbon nanotubes. *Nano Lett.* **2021**, *21*, 3134−3138.
(52) Yu, W.; Zhao, X.; Jiang, P.; Liu, C.; Yang, R. Tunable anisotropic thermal transport in super-aligned carbon nanotube films. *Mater. Today Phys.* **2021**, *20*, No. 100447.

https://doi.org/10.1021/acsami.4c07913
ACS Appl. Mater. Interfaces 2024, 16, 45671−45677